Diagnosis of the Warm Rain Process in Cloud-Resolving Models Using Joint *CloudSat* and MODIS Observations

KENTAROH SUZUKI*

Department of Atmospheric Science, Colorado State University, Fort Collins, Colorado

GRAEME L. STEPHENS

Jet Propulsion Laboratory, California Institute of Technology, Pasadena, California

SUSAN C. VAN DEN HEEVER

Department of Atmospheric Science, Colorado State University, Fort Collins, Colorado

TAKASHI Y. NAKAJIMA

Research and Information Center, Tokai University, Tokyo, Japan

(Manuscript received 28 December 2010, in final form 3 June 2011)

ABSTRACT

This study examines the warm rain formation process in global and regional cloud-resolving models. Methodologies developed to analyze *CloudSat* and Moderate Resolution Imaging Spectroradiometer (MODIS) satellite observations are employed to investigate the cloud-to-precipitation processes and are applied to model results for comparisons with corresponding statistics from the observations. Three precipitation categories of no precipitation, drizzle, and rain are defined according to nonattenuated near-surface radar reflectivity, and their fractional occurrences and the probability of precipitation are investigated as a function of cloud properties such as droplet size, optical thickness, droplet number concentration, and liquid water path. The comparisons reveal how the models are qualitatively similar to, but quantitatively different from, observations in terms of cloud-to-rainwater conversion processes. Statistics from one model reveal a much faster formation of rain than observed, with drizzle occurrence being much less frequent, whereas statistics from the other model illustrate rain formation closer to satellite observations but still faster formation of drizzle water. Vertical profiles of radar reflectivity that are rescaled as a function of in-cloud optical depth and classified according to particle size are also compared. The results show that each model indicates systematically faster formation of rain and drizzle, respectively, than observed in vertical profiles although they indicate that the cloud-to-rain transitions are qualitatively similar to observations. These results characterize the model behavior in terms of warm cloud microphysics and then point to a possible area of model improvement for more realistic representation of warm rain formation processes.

1. Introduction

Cloud-related processes are recognized as one of the main sources of uncertainty in understanding and predicting global climate change (e.g., Stephens 2005; Dufresne and Bony 2008). Warm liquid clouds are of particular importance in the earth's climate for their significant effects on the hydrologic cycle and energy budget. The rate at which liquid precipitation falls from warm clouds is in part controlled by the microphysical growth processes of cloud particles. Liquid cloud particles are formed through the nucleation of aerosols serving as cloud condensation nuclei (CCN) and then grow through condensation and coalescence processes and are also subject to evaporation processes (Rogers and Yau 1989). These processes determine the precipitation

* Current affiliation: Jet Propulsion Laboratory, California Institute of Technology, Pasadena, California.

Corresponding author address: Kentaroh Suzuki, Jet Propulsion Laboratory, California Institute of Technology, Mail Stop 233-300, 4800 Oak Grove Drive, Pasadena, CA 91109.
E-mail: kentaro.suzuki@jpl.nasa.gov

DOI: 10.1175/JAS-D-10-05026.1

rate and the microphysical structure of the clouds that are important for their hydrological and radiative effects. The conversion process of cloud water into rainwater is characterized by the time scale of the process. Factors that determine the time scale of this process, however, are not well understood (e.g., Khain et al. 2000), especially on the global scale. These water conversion processes are usually represented in numerical weather and climate prediction models by bulk parameterization schemes developed in terms of the mass and number densities of cloud water and rainwater. To improve our understanding and prediction of the precipitation formation process, it is essential to evaluate how realistically these microphysical parameterizations represent the cloud-to-rain conversion processes.

For such an evaluation, it is important to gather cloud-scale observations of the warm rain processes on the global scale. Notable in this regard is the recent emergence of *CloudSat* (Stephens et al. 2008) that carries the W-band Cloud Profiling Radar (CPR), providing a new tool for observing cloud processes on the global scale. *CloudSat* also flies as part of constellation of satellites referred to as the A-Train (Stephens et al. 2002), which includes the *Aqua* satellite equipped with Moderate Resolution Imaging Spectroradiometer (MODIS) visible/infrared radiometers and Advanced Microwave Scanning Radiometer for the Earth Observing System (AMSR-E) microwave imagers. The combined use of these active and passive sensors included in A-Train has indeed provided new insights into the cloud-to-precipitation processes (Stephens and Haynes 2007; Suzuki and Stephens 2008; Leon et al. 2008; Kubar et al. 2009; Nakajima et al. 2010a; Suzuki et al. 2010) and their probable link to aerosols (Lebsock et al. 2008; Berg et al. 2008; L'Ecuyer et al. 2009; Saleeby et al. 2010).

The *CloudSat* CPR is also capable of detecting precipitation (Haynes et al. 2009) and this capability has also been employed for model comparisons (Stephens et al. 2010). The results highlighted major biases of model precipitation with the fact that the bias is also found in a global cloud-resolving model (CRM) simulation with much finer horizontal resolution of 7 km than other traditional climate models. This implies that the biases are caused not only by coarse resolution but also by uncertainties in parameterizations of the warm rain processes. Our recent study (Suzuki and Stephens 2009) also showed that the time scale of warm rain formation is significantly shorter in the model than implied from *CloudSat*.

For investigating the model precipitation, it is therefore necessary to evaluate the cloud-to-rainwater conversion process of models more directly. Notable in this regard are recent innovations in observational analysis mentioned above that use *CloudSat* and A-Train multisensor measurements to examine warm cloud microphysical processes. Some of these analyses (Lebsock et al. 2008; L'Ecuyer et al. 2009) found that the probability of precipitation (POP), defined as the fractional occurrence of precipitation events with precipitation rate greater than a threshold value, tends to increase monotonically with cloud liquid water path (LWP) and is significantly modified by aerosol abundance, illustrating how the cloud-to-rainwater conversion process occurs and how it tends to be affected by aerosols. Another approach (Suzuki et al. 2010) examined the *CloudSat* vertical radar profiles rescaled as a function of in-cloud optical depth and found how the cloud-to-rain vertical transitions vary systematically with variations in MODIS-derived particle size. These studies demonstrate how to exploit the multisensor observations of the A-Train to examine microphysical processes, bringing a new piece of observational information to be used for comparisons with model statistics.

In this study, we apply these analysis methods to model output and compare the results with corresponding statistics from A-Train observations in order to evaluate the model representations of warm rain processes and to better understand the observed characteristics of the warm rain statistics. Since the methods introduced above are capable of examining microphysical processes in depth, such comparisons are expected to provide a useful diagnosis of model behaviors in terms of the warm rain process. This study intends to demonstrate how to utilize the *CloudSat*/A-Train multisensor observations for such a model diagnosis as well as how to use models to explain the observations by performing the comparisons using simulation results from global and regional CRMs as a test bed. The models examined are (i) the Nonhydrostatic Icosahedral Atmospheric Model (NICAM) global CRM (e.g., Tomita and Satoh 2004; Satoh et al. 2008) and (ii) the Regional Atmospheric Modeling System (RAMS) regional CRM (e.g., Pielke et al. 1992; Cotton et al. 2003). These two models differ not only in their spatial scales but also in their horizontal resolutions and representations of cloud microphysical processes. Differences in the statistics from the two models would provide a hint as to how different model setups and parameterizations may influence the warm rain statistics. This study intends to demonstrate how to use the *CloudSat* and MODIS observations in assessing warm rain statistics for a range of different model setups, instead of a direct comparison between different models with different microphysics schemes. It is also worth noting that the warm rain statistics examined in this study are dictated by combined effects of various microphysical processes such as autoconversion, accretion, evaporation,

and sedimentation. The comparisons shown should be interpreted as a diagnosis of the overall characteristic of warm rain processes rather than a focus on any specific single process. The analysis methods mentioned above, however, are still able to capture essential aspects of the cloud-to-precipitation processes as demonstrated by the previous studies, and thus comparisons between the models and observations would contribute to better diagnosis of the model microphysics parameterizations.

In this paper, we first describe the satellite data in section 2 and the models employed in this study in section 3. The analysis methods mentioned above are reviewed and then applied to comparisons of warm rain characteristics between observations and the models in section 4. In section 5, we summarize the findings of this study and provide a discussion on how to interpret the results in terms of model behaviors with regard to warm cloud microphysics.

2. Satellite data

a. CloudSat

The first satellite data used in this study are the data products of the *CloudSat* mission. We employ radar reflectivity profiles from the 2B-GEOPROF product (e.g., Mace et al. 2007; Marchand et al. 2008) and precipitation rates from the 2C-PRECIP-COLUMN product (Haynes et al. 2009). We also employ the precipitation flag contained in the 2C-PRECIP-COLUMN product. This flag categorizes warm rain characteristics according to near-surface nonattenuated radar reflectivity values Z_{sfc} estimated from the path-integrated attenuation (PIA) by the method of Haynes et al. (2009). The pixel-by-pixel data of these products for the period of June–August (JJA) 2006 are employed in this study. Only pixels over the global ocean are used since the 2C-PRECIP-COLUMN product is limited to oceanic regions because of the difficulty in estimating PIA over land surface (Haynes et al. 2009). The information about drizzle and precipitation obtained from these *CloudSat* products is combined with cloud properties derived from MODIS shortwave retrievals that are described below in next subsection.

b. MODIS

We also employ cloud properties—cloud droplet effective radius (CDR) and cloud optical thickness (COT)—obtained from MODIS shortwave measurements. These cloud properties are provided by MODIS retrievals matched to the *CloudSat* radar footprint (Nakajima et al. 2010a) and are based on the algorithm of Nakajima and Nakajima (1995) enhanced by Kawamoto et al. (2001). It is worth noting that there are two kinds of effective particle radius obtained from *Aqua*/MODIS 2.1- and 3.7-μm channels. These tend to characterize different optical depth within the cloud layer (Nakajima et al. 2010a; Suzuki et al. 2010) as theoretically demonstrated by previous studies (e.g., Platnick 2000; Chang and Li 2002). We only employ effective particle radius retrieved from the 2.1-μm channel for model comparisons in this study since the differences in statistics between effective radii from 2.1- and 3.7-μm channels are much smaller than those between observations and the models.

3. The models

a. NICAM

The first model investigated in this study is the NICAM global CRM developed by Tomita and Satoh (2004) and Satoh et al. (2008). The NICAM model has been employed for several types of global cloud-resolving simulations including a simulation of the Madden–Julian oscillation (MJO) event (Miura et al. 2007) with horizontal resolution of up to 3.5 km. Although several studies have shown that the spatiotemporal occurrences of clouds and precipitation are in general well reproduced by the model in comparison with satellite observations (Masunaga et al. 2008; Satoh et al. 2010; Inoue et al. 2010), these studies have paid much less attention to warm cloud microphysical processes, which have not yet been coupled to aerosol effects. Under these circumstances, Suzuki et al. (2008) have recently implemented the aerosol transport module from the Spectral Radiation Transport Model for Aerosol Species (SPRINTARS) aerosol model (Takemura et al. 2000, 2002) into NICAM to represent aerosol–cloud interaction processes in the global CRM. In this aerosol-coupled version of NICAM, which is referred to as NICAM-SPRINTARS, the aerosol effects are incorporated into cloud microphysical and radiative transfer processes so that the direct and indirect effects (the first and second kinds) of aerosols are represented (Suzuki et al. 2008). Suzuki et al. (2008) then performed a global simulation with horizontal resolution of 7 km and time step of 30 s for the period of 1–8 July 2006. This horizontal resolution makes the best use of the state-of-the-art computational resources of the Earth Simulator given extra memory use for aerosol species in addition to variables in the NICAM standard version. Suzuki et al. (2008) showed that the cloud properties and their interactions with aerosols are generally well simulated on the global scale in comparison with MODIS satellite observations, including the detailed spatial structure of CDR, correlation statistics of cloud properties with aerosols, and vertical growth patterns of cloud droplets. The present study utilizes the simulated data over the global ocean from this aerosol-coupled version

of NICAM, or NICAM-SPRINTARS. A novel feature of NICAM-SPRINTARS, especially when compared to the standard version of NICAM without aerosols, is variability of cloud properties as a function of aerosol amount, which is also a variable predicted in the model and thus has inhomogeneous spatiotemporal distributions. This variability, which the NICAM standard version lacks, enables us to make statistics of precipitation in relation to cloud properties that vary over a range comparable to that in the real atmosphere. This study therefore provides a first opportunity for meaningful evaluation of warm cloud microphysics in the NICAM model.

The aerosol effects are treated in NICAM-SPRINTARS as described below. The SPRINTARS aerosol transport module predicts mass mixing ratios of main aerosol species, namely sulfates, carbonaceous aerosols (black carbon and organic carbon), soil dust, and sea salt as described in Takemura et al. (2000). The carbonaceous aerosols are treated as internal mixtures of black carbon and organic carbon with varying ratios and the mixtures among different species are treated as external mixtures. The mass mixing ratios are converted into number concentrations through assumed size distributions and mode radii. The total aerosol particle number concentration N_a is then employed to estimate cloud droplet number concentration N_c at each grid point through an empirical relationship between N_a and N_c as introduced by Suzuki et al. (2004). The number concentration thus obtained is further used in the cloud physics scheme to compute the autoconversion rate from cloud water into rainwater.

The cloud physics scheme in this version of NICAM-SPRINTARS is based on a single-moment scheme of Grabowski (1998) that represents the warm rain process by parameterizations of both autoconversion and accretion processes. The cloud-to-rainwater conversion rate in Grabowski (1998) is formulated in terms of time scales of these processes as (Suzuki and Stephens 2009)

$$\frac{\partial(\rho q_r)}{\partial t} = -\frac{\partial(\rho q_c)}{\partial t} = \left(\frac{1}{\tau_{\text{aut}}} + \frac{1}{\tau_{\text{acc}}}\right)\rho q_c,$$

where q_c and q_r are the cloud and rainwater mixing ratios, respectively, ρ denotes atmospheric density, and τ_{aut} and τ_{acc} represent the time constant of autoconversion and accretion, respectively. These time constants are further parameterized as

$$\tau_{\text{aut}}(\rho q_c, N_c) = \frac{\beta + \gamma N_c/[\rho q_c \sigma(N_c)]}{\alpha \rho q_c},$$
$$\tau_{\text{acc}}(\rho q_r, N_r) = cN_r^{-1/6}(\rho q_r)^{-5/6}, \quad (1)$$

where $\sigma(N_c) = 0.146 - 5.964 \times 10^{-2} \times \ln(N_c/2000)$, N_c and N_r denote the number concentration of cloud and rain particles, respectively, and $\alpha = 1.67 \times 10^{-5}$, $\beta = 5$, and $\gamma = 0.036$ are prescribed constants in the MKS system of units. Also, c is a constant that is given as

$$c^{-1} = c_r E_r \pi \left(\frac{3}{\pi\rho_w}\right)^{2/3}\left(\frac{6}{\pi\rho_w}\right)^{1/6},$$

where ρ_w is liquid water density, $E_r = 0.8$ is collection efficiency, and $c_r = 130$ is a prescribed constant [see Grabowski (1998) and Suzuki and Stephens (2009) for more detailed derivations]. The warm rain thus formed determines the cloud water content ρq_c remaining after the precipitation occurs. The effective particle radius r_e at each grid point is then computed from ρq_c and N_c as

$$r_e = k^{-1/3}\left(\frac{3}{4\pi\rho_w}\frac{\rho q_c}{N_c}\right)^{1/3},$$

where k represents the factor relating volume-mean radius to effective radius and is assumed to be $k^{-1/3} = 1.1$. The CDR near the cloud top is then determined as the value at the highest level where ρq_c is greater than a threshold value of 0.1 g m^{-3}. The warm clouds are also defined using temperature T at the cloud top and are determined as those with $T > 273$ K. The cloud optical thickness τ_c is also computed from r_e and q_c at each height according to its definition as

$$\tau_c = \frac{3}{2\rho_w}\int \frac{\rho q_c}{r_e} dz.$$

The cloud properties thus determined were shown to have spatial structures and correlation patterns with aerosols similar to those observed by MODIS on the global scale (Suzuki et al. 2008). These cloud properties as well as surface precipitation rate are used to construct statistics that are compared with A-Train observations as presented below in section 4.

b. RAMS

The second model examined is the RAMS regional CRM (Pielke et al. 1992; Cotton et al. 2003). The recent study of van den Heever et al. (2011) performed a two-dimensional large-domain and long-duration idealized simulation under conditions of radiative–convective equilibrium (RCE) over ocean surface. They conducted sensitivity experiments of changing aerosol conditions to investigate aerosol effects on tropical convection. This study utilizes the model data from their simulations. A striking difference between RAMS and NICAM is not only their spatial scales but also their representations of cloud microphysics. The RAMS model adopts a two-moment bulk microphysics scheme that predicts number

concentrations and mass mixing ratios of hydrometeors. The scheme is based on Meyers et al. (1997) but enhanced by Feingold et al. (1998) and Feingold and Heymsfield (1992). The enhancements attempt to represent the essence of size-resolved bin microphysics models through introducing a lookup table approach that emulates the detailed microphysics computations within a framework of bulk microphysics.

The RAMS microphysics scheme represents cloud and rain size spectra using basis functions such as log-normal and gamma functions. Four prognostic variables are required to describe the two basis functions (i.e., cloud and rain) for warm rain processes. The two moments of each basis function (i.e., number and mass concentration) are predicted for this purpose. In this scheme, the autoconversion and accretion processes are represented by interactions within each water category as well as among categories (i.e., cloud–cloud, cloud–rain, and rain–rain interactions). The rate of change in mass and number concentrations for the cloud and rain categories due to these interactions is facilitated through the use of lookup table. The table stores the results computed from a spectral-bin microphysics model for the assumed basis functions over a variety of number and mass concentration values. The simulation of van den Heever et al. (2011) assumed a modified-gamma function with fixed shape parameter $\mu = 2$ for the cloud and rain basis functions. The cloud microphysics is also coupled with aerosols through nucleation in a way that represents CCN activation based on Köhler theory as described in Saleeby and Cotton (2004).

The RCE simulations were performed for 100 days and the results for the last 40 days are employed for analysis in this study because it took 60 days for the model to achieve an RCE state. The experiments with perturbed aerosol amount were run from day 60 until day 100 (van den Heever et al. 2011). The horizontal resolution of these simulations is 1 km and the vertical grid consists of 36 levels with stretched grid spacing where 8 levels are found within the lowest 1-km layer. The computational domain is 10 000 km in the horizontal and 26 km in the vertical, and the time step is 10 s. The difference in time step between NICAM and RAMS is unlikely to influence the difference in time rates of cloud-to-rainwater conversion that will be shown in next section since the time steps of the models are both significantly shorter than typical time scale of warm rain formation in the models ($\sim 10^3$–10^4 s). Other details of the model configuration and simulation setup are described in van den Heever et al. (2011). In this study, we compute the near-cloud-top effective particle sizes and cloud optical thickness from cloud water mixing ratios and number concentrations provided by this simulation in a manner similar to those for NICAM described above. The cloud properties thus obtained, as well as the surface precipitation rate, are then employed to construct warm rain statistics that are compared with those from NICAM and A-Train observations as shown below in the next section.

4. Warm rain analysis

a. Radar reflectivity simulation

For comparing model statistics with *CloudSat* and A-Train observations in a consistent way, it is useful to translate the model output into observed quantities measured by satellite sensors. For this purpose, we simulate radar reflectivity factors using the QuickBeam radar simulator (Haynes et al. 2007) applied to output from NICAM and RAMS. The size distribution functions of cloud and rainwater species are assumed to be modified-gamma and exponential functions, respectively, to simulate radar reflectivity for NICAM, following the assumption of Grabowski (1998), although there is no explicit assumption for cloud water in Grabowski (1998). For RAMS simulations, a modified-gamma function is assumed for all the hydrometeors species for consistency with assumptions in the original simulation of van den Heever et al. (2011). These simulations of radar reflectivity incorporate the effect of attenuation due to hydrometeors (especially rain particles) so that the simulated values are directly comparable to *CloudSat* observations.

b. Occurrence of drizzle and rain

To examine the rain formation process, we first investigate the occurrence of drizzle and rain using the *CloudSat* 2C-PRECIP-COLUMN product (Haynes et al. 2009). There are four categories of precipitation occurrence defined in this product for this purpose. These flags are defined according to the near-surface nonattenuated radar reflectivity $Z_{\rm sfc}$: (i) no precipitation, (ii) rain possible, (iii) rain probable, and (iv) rain certain, corresponding to $Z_{\rm sfc} < -15$ dBZ, $-15 < Z_{\rm sfc} < -7.5$ dBZ, $-7.5 < Z_{\rm sfc} < 0$ dBZ, and $Z_{\rm sfc} > 0$ dBZ, respectively. Although L'Ecuyer et al. (2009) examined fractional occurrences of these categories as a function of AMSR-E LWP, we combine for simplicity the categories (ii) and (iii) into a single category defined as $-15 < Z_{\rm sfc} < 0$ dBZ and now referred to as the drizzle category. We therefore have three categories of (i) no precipitation, (ii) drizzle, and (iii) rain, corresponding to $Z_{\rm sfc} < -15$ dBZ, $-15 < Z_{\rm sfc} < 0$ dBZ, and $Z_{\rm sfc} > 0$ dBZ, respectively.

Figure 1 shows global geographical distributions of the fractional occurrences of each category obtained

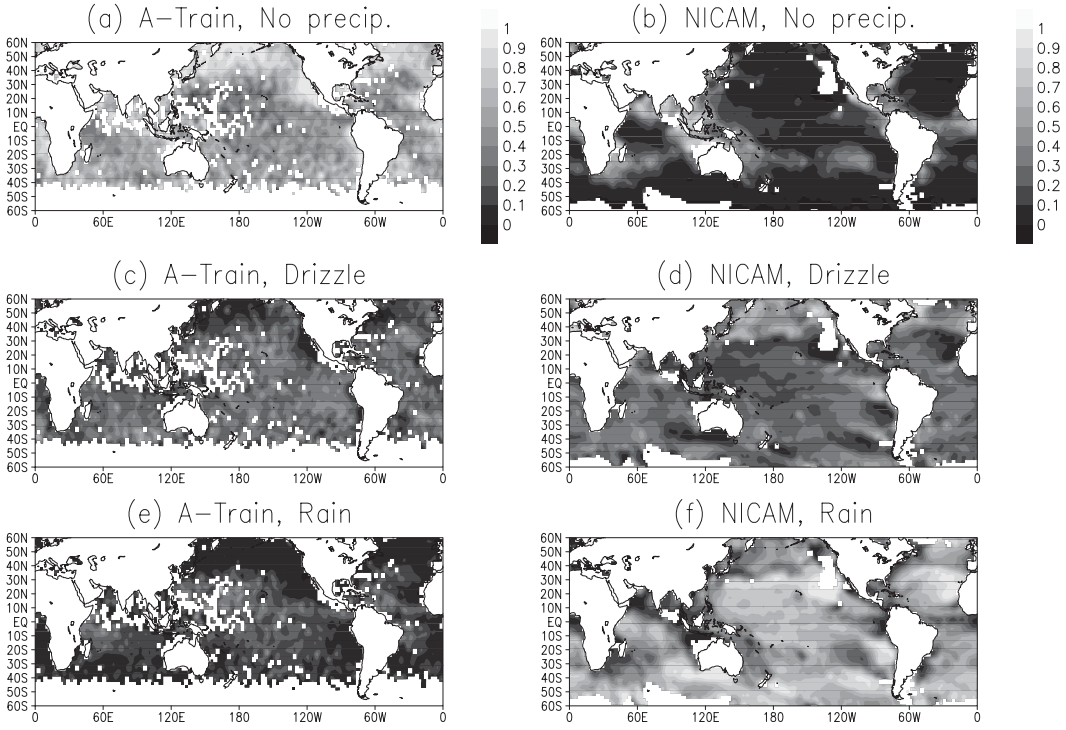

FIG. 1. Global geographical distributions of fractional occurrence of (a),(b) no precipitation, (c),(d) drizzle, and (e),(f) rain categories obtained from (a),(c),(e) A-Train observations and (b),(d),(f) the NICAM-SPRINTARS model.

from *CloudSat* in comparison with NICAM statistics. Fractional occurrences shown here are for warm clouds with optical thickness greater than 10, highlighting drizzle and rain global statistics from A-Train and NICAM for relatively thick clouds. NICAM tends to produce significantly smaller fractions of the no precipitation category and larger fractions of the drizzle and rain categories compared to A-Train observations. Figure 1 also reveals noticeable differences between *CloudSat* and NICAM in the geographical distributions of occurrences for each category. These differences suggest that the partitioning among cloud, drizzle, and rain in NICAM have systematic biases compared to those in the real atmosphere on the global scale. It is also interesting to find that the distribution of the NICAM drizzle category (Fig. 1d) tends to be more similar to that of the *CloudSat* no precipitation category (Fig. 1a) than to that of the *CloudSat* drizzle category (Fig. 1c). Similarly, the distribution of the NICAM rain category (Fig. 1f) appears to resemble that of the *CloudSat* drizzle category (Fig. 1c) rather than that of the *CloudSat* rain category (Fig. 1e). These characteristics suggest that NICAM's warm rain occurrence at a given spatial point is ''shifted'' to larger precipitation rates compared to *CloudSat* observations. The regional characteristics of the precipitation occurrence are influenced by environmental conditions such as static stability and aerosol amount, and the difference between the model and observation implies a difference in precipitation response to these environmental factors. More detailed analysis of such regional characteristics and their probable link to the environmental conditions would be valuable to perform in future studies based on findings of the present study.

To understand possible causes for this systematic model bias in terms of cloud microphysical processes, we investigate fractional occurrences of each precipitation category as a function of LWP. Figure 2 shows comparisons of A-Train, NICAM, and RAMS for such a statistic. For A-Train observations, the LWP W is computed from MODIS-retrieved CDR r_e and COT τ_c according to

$$W = \frac{2}{3}\rho_w r_e \tau_c.$$

For the models, LWPs are computed as a vertical integral of cloud water content.

The A-Train observation shown in Fig. 2a illustrates how the cloud-to-rainwater conversion occurs as a function of LWP in the real atmosphere. The fraction of the no precipitation category (red curve) tends to decrease monotonically with increasing LWP. The fraction

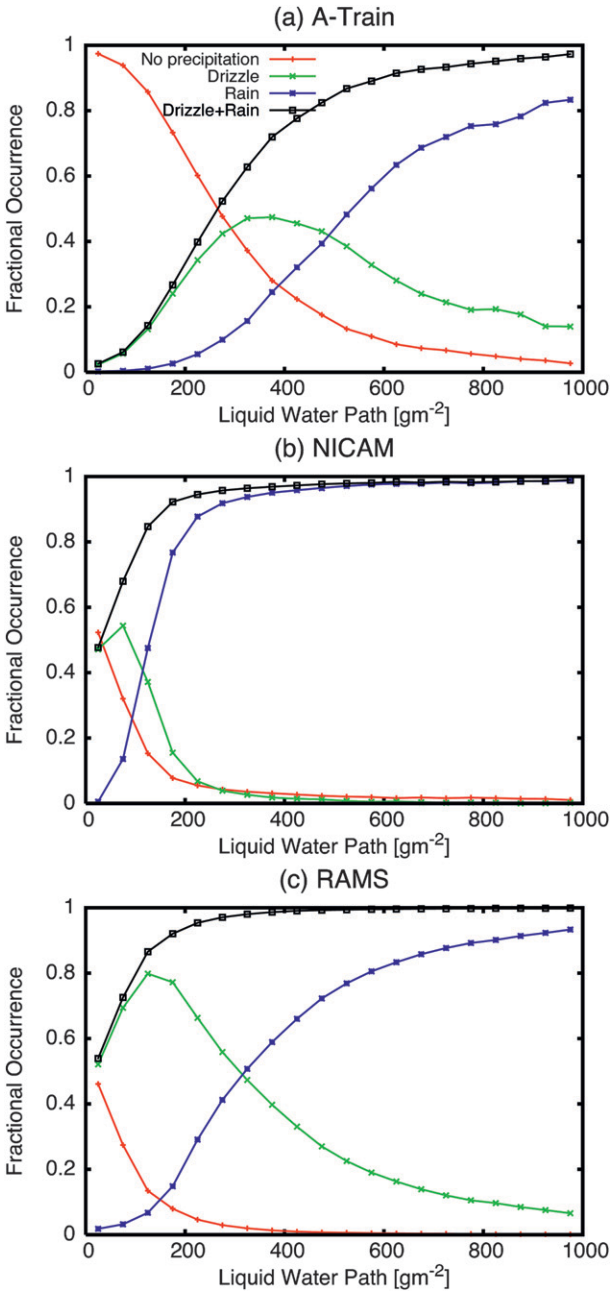

FIG. 2. Fractional occurrence of no precipitation (red), drizzle (green), and rain (blue) categories as a function of cloud LWP obtained from (a) A-Train, (b) NICAM-SPRINTARS, and (c) RAMS. Shown in black is the sum of contributions from drizzle and rain categories.

of drizzle (green curve) at first increases around intermediate values of LWP and then decreases with increasing LWP as this mode of precipitation shifts to the rain category with increasing LWP. This is illustrated by the way the fraction of the rain category, indicated by the blue curve, monotonically increases with increasing LWP. These tendencies demonstrate how the transitions from cloud through drizzle to rain tend to occur smoothly as a monotonic function of LWP as noted also by Lebsock et al. (2008) and L'Ecuyer et al. (2009). It is worth noting that the results shown here based on MODIS LWP are closely similar to those of Lebsock et al. (2008) and L'Ecuyer et al. (2009), which are based on AMSR-E microwave LWP. This similarity implies that these tendencies of drizzle and rain occurrences as a function of LWP are relatively robust.

The model statistics from NICAM (Fig. 2b) and RAMS (Fig. 2c) are systematically different from one another as well as from the A-Train observations although these two models tend to represent qualitative characteristics of the water conversion from cloud through drizzle to rain as a function of LWP. The NICAM results (Fig. 2b) show much reduced fractions of no precipitation and drizzle and much larger occurrences of rain than observed, even for smaller values of LWP, thus illustrating how the water conversion process takes place much faster than reality. This has been pointed out previously by Suzuki and Stephens (2009). This deficiency tends to be improved in the RAMS results (Fig. 2c) that show fractional occurrences of rain much closer to A-Train observations than in NICAM. The fractional occurrence of the drizzle category in RAMS increases with LWP at low LWP and eventually decreases with increasing LWP, which is qualitatively similar to A-Train observations. The RAMS drizzle, however, has a systematic bias compared to the A-Train observations. The drizzle fraction in RAMS tends to increase with increasing LWP more quickly than in observations, suggesting that the cloud-to-drizzle conversion occurs faster in RAMS than in the real atmosphere. This faster cloud-to-drizzle transition in RAMS makes the absolute fractions of drizzle occurrence significantly larger than observed and also makes the fractions of the no precipitation category as small as those in NICAM.

When the fractions of the drizzle and rain categories are summed as shown in the black curves of Fig. 2, a common characteristic of both models is revealed. The combined fractions of the drizzle and rain categories (or equivalently the fraction of the no precipitation category) are similar: both NICAM and RAMS tend to more quickly convert cloud water into larger-sized hydrometeors. These larger-sized hydrometeors are mainly in the rain category in NICAM and are initially in the drizzle category but then transition to rain in RAMS. The drizzle-to-rain transition in RAMS appears to be more realistic than in NICAM, making the RAMS fraction of the rain category much closer to observations. These results simply illustrate characteristics of these models in terms of cloud-to-rainwater conversion processes.

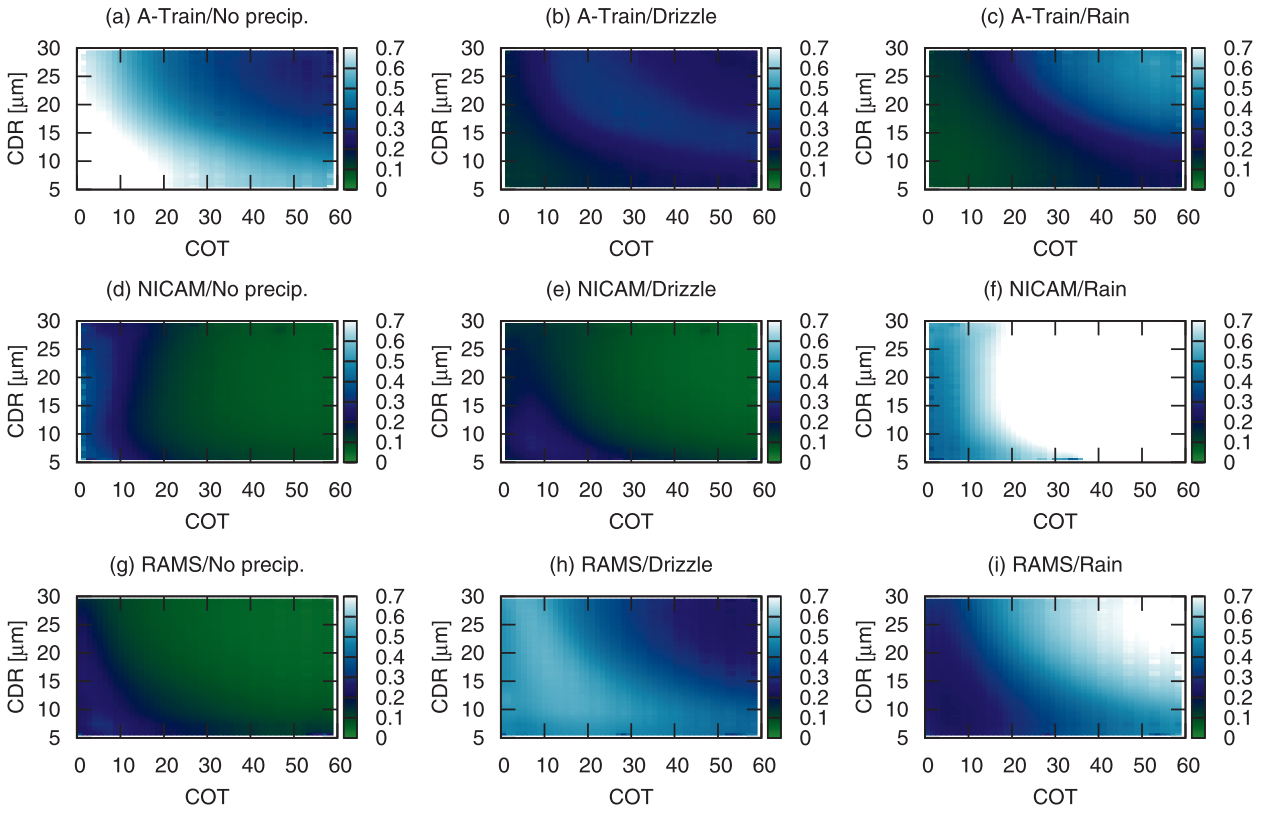

FIG. 3. Fractional occurrence of (a),(d),(g) no precipitation, (b),(e),(h) drizzle, and (c),(f),(i) rain categories as a function of CDR and COT obtained from (a)–(c) A-Train, (d)–(f) NICAM-SPRINTARS, and (g)–(i) RAMS.

Given that the statistics shown are based on precipitation categorization with thresholds of −15 and 0 dBZ, these characteristics shown in Fig. 2 are considered to be robust for uncertainties in radar reflectivity within the order of decibels. The *CloudSat* measurement has an accuracy of approximately 2 dB as determined by radiometric calibration (Tanelli et al. 2008). In the model simulations, radar reflectivity is roughly proportional to the square of mass mixing ratio and inversely proportional to number density, and their uncertainties of a factor of 2 approximately correspond to a reflectivity uncertainty of several decibels.

These characteristics of the models are further investigated by analyzing the fractional occurrence of the precipitation categories as a function of CDR and COT obtained from MODIS shortwave analysis. Although CDR and COT can be translated into number concentration and LWP as will be shown below, CDR and COT are two primary quantities observed by shortwave remote sensing in general (e.g., Nakajima and King 1990). Such an analysis provides more detailed examination of warm rain formation than is shown in Fig. 2 in terms of cloud properties in the two-dimensional plane defined by CDR and COT. Shown in Fig. 3 is such a comparison of A-Train (Figs. 3a–c), NICAM (Figs. 3d–f), and RAMS (Figs. 3g–i) for no precipitation (left panels), drizzle (middle panels), and rain categories (right panels). Figure 3a illustrates that the no precipitation category in the A-Train observations mainly occurs over the lower left region of the CDR-COT plane, which corresponds to smaller values of CDR and COT. The drizzle category is mainly found to appear in intermediate region of the plane (Fig. 3b), and the rain category takes place over the upper-right region for larger values of CDR and COT (Fig. 3c). These A-Train results illustrate how drizzle and rain occurrences systematically transition with variations of CDR and COT. Figures 3d–f show corresponding statistics from NICAM, which illustrates that the no precipitation category hardly occurs (Fig. 3d) and the drizzle category is also infrequent and takes place over smaller CDR and COT values (Fig. 3e), making the rain category the prevailing mode of the CDR-COT plane (Fig. 3f). The RAMS statistics shown in Figs. 3g–i also tend to be systematically different from either the A-Train or NICAM. The occurrence of the no precipitation category (Fig. 3g) is much less frequent than the A-Train observations similar to NICAM, whereas the drizzle category tends to be dominant especially

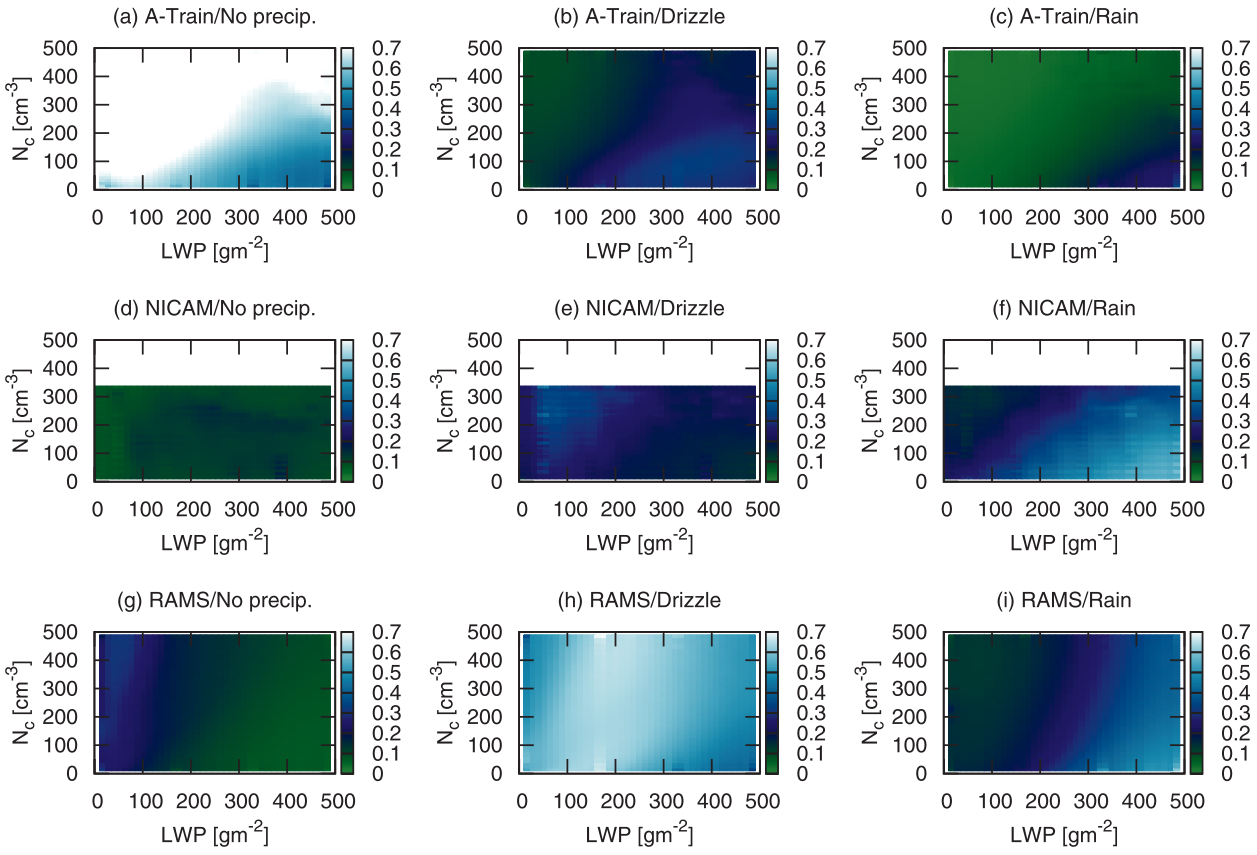

FIG. 4. As in Fig. 3, but as a function of CDNC and LWP.

over the lower-left region of the CDR-COT plane (Fig. 3h), with fractions much larger than A-Train and NICAM. The rain category is then found to occur with amplitudes closer to the A-Train than in NICAM, as shown in Fig. 3i. These characteristics of the RAMS statistics suggest that the cloud water tends to be converted into drizzle water much more quickly than observed, which then transitions to rainwater in a more appropriate manner than in NICAM. These features shown in Fig. 3 confirm the striking differences in warm rain characteristics among the A-Train, NICAM, and RAMS.

Since the primary prognostic variables in models are mass mixing ratio and number concentration and their cloud physics parameterization schemes are typically formulated in terms of these quantities as in (1), it is useful, from the modeling point of view, to investigate the fractional occurrences of precipitation categories as a function of cloud droplet number concentration (CDNC) and LWP as shown in Fig. 4. For this purpose, the CDNC and LWP are estimated from CDR and COT by invoking the adiabatic growth model (e.g., Brenguier et al. 2000; Bennartz 2007) for A-Train observations. For model statistics, the CDNCs are estimated as vertically averaged values and the LWPs are computed by vertically integrating the cloud water content for warm-topped liquid cloud layers. Figures 4a–c illustrate how the occurrences of the precipitation categories tend to systematically vary with CDNC and LWP in a manner translated from Figs. 3a–c. The corresponding statistics from NICAM shown in Figs. 4d–f again demonstrate that the no precipitation category hardly takes place (Fig. 4d) and the drizzle category (Fig. 4e) tends to occur for smaller LWP and larger CDNC ranges than observed, causing the rain category to prevail in the CDNC-LWP plane. In the case of RAMS, shown in Figs. 4g–i, the CDNC-LWP plane is dominated by the drizzle category (Fig. 4h) and the rain category occurrence is closer to A-Train (Fig. 4i). The occurrence of the no precipitation category (Fig. 4g) is again much smaller than observed similarly to NICAM. Although Fig. 4 exposes these discrepancies between observations and the models, qualitative similarities can also be found in Fig. 4. According to Figs. 4a–c, the contours for specific values of the fractional occurrence are found to be tilted so that dependencies of the fractional occurrences on LWP vary

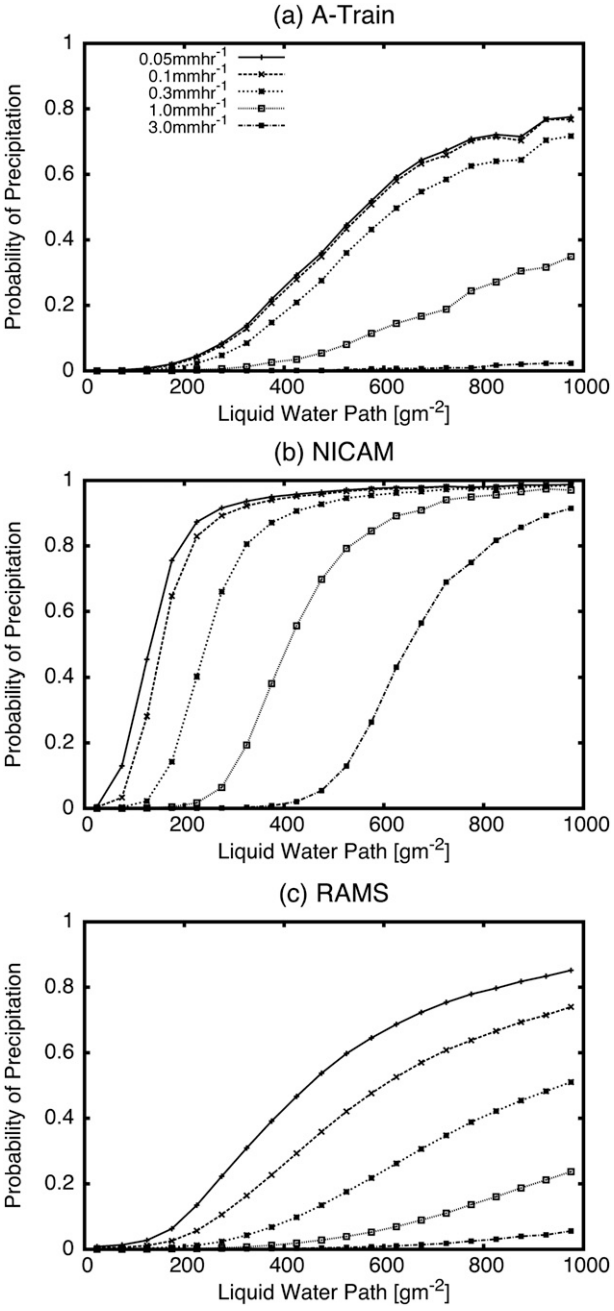

FIG. 5. POP defined with specified threshold values of precipitation rate as a function of LWP obtained from (a) A-Train, (b) NICAM-SPRINTARS, and (c) RAMS.

systematically with CDNC. This variation illustrates how the relationships shown in Fig. 2 tend to change with CDNC. It is then worth noting that such a variation is also represented in the NICAM and RAMS statistics as shown in Figs. 4d–f and 4g–i, respectively, where contours for specific values of the fractional occurrences also tend to be tilted in a manner qualitatively similar to A-Train observations. This suggests that the parameterizations employed in NICAM and RAMS tend to represent the qualitative behavior of drizzle and rain formation as a function of CDNC and LWP, although the models have their own systematic biases in a quantitative sense.

c. *Rainfall characteristics of precipitating clouds*

To understand the model behavior regarding the warm rain formation in more detail, we now investigate the characteristics of precipitating clouds, defined as those belonging to the rain category. Although the rain category is defined according to the surface radar reflectivity as explained above, more detailed analysis focusing on precipitating clouds requires further breakdown into subcategories within the rain category according to surface rainfall rate. For this purpose, the rain category is further divided into subcategories according to surface precipitation rate obtained from the 2C-PRECIP-COLUMN product (Haynes et al. 2009) for observational analysis and simulated by the models for model statistics. Figure 5 shows POP as a function of LWP for different threshold values of precipitation rate obtained from A-Train (Fig. 5a), NICAM (Fig. 5b), and RAMS (Fig. 5c). The POPs are defined as fractional occurrences of precipitation events with precipitation rates greater than given threshold values shown in Fig. 5. The A-Train observations (Fig. 5a) show that the POP tends to monotonically increase with increasing LWP and the POP becomes systematically smaller as the threshold values of precipitation rate increase. The NICAM statistics (Fig. 5b) clearly illustrate much faster production of precipitation from cloud water for all of the threshold values of precipitation rate, consistent with results shown above. The RAMS statistics (Fig. 5c), by contrast, are much closer to A-Train observations, suggesting that the precipitating clouds in RAMS tend to produce rainfall from cloud water more realistically.

Figure 6 shows the comparisons of POPs for the A-Train, NICAM, and RAMS as a function of CDR and COT for selected threshold values of precipitation rate. The A-Train observations (Figs. 6a–c) show that the POP for a specific threshold value tends to increase with increasing CDR and COT. The absolute values of POP for larger threshold values are also found to be smaller. These observational statistics conveniently illustrate how precipitation characteristics tend to relate to cloud properties in the real atmosphere. These behaviors are also found in model statistics of NICAM (Figs. 6d–f) and RAMS (Figs. 6g–i), at least in a qualitative manner, although NICAM is found to be biased toward larger absolute values of POP. This feature of the NICAM statistics confirms its biases in warm rain formation shown

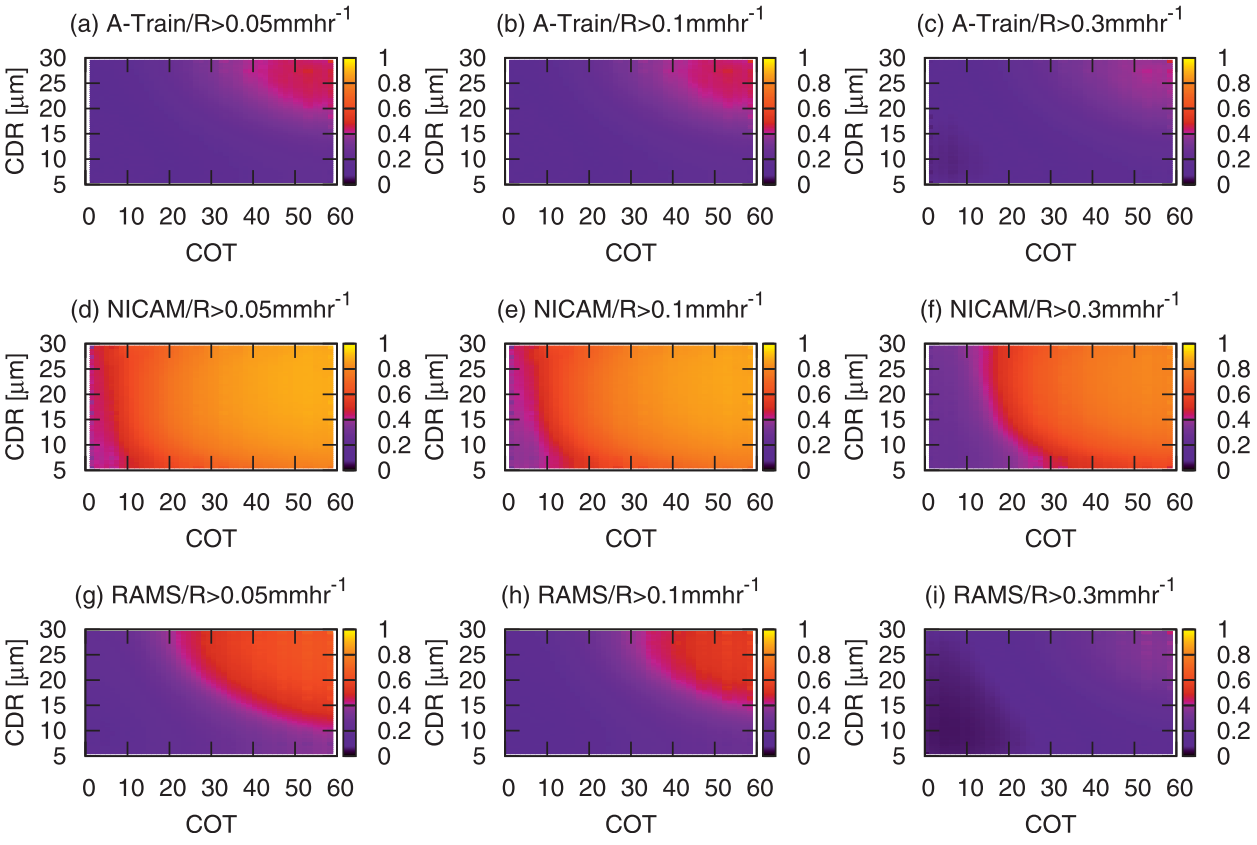

FIG. 6. POP defined with specified threshold values of precipitation rate of (left to right) 0.05, 0.1, and 0.3 mm h^{-1} as a function of CDR and COT obtained from (a)–(c) A-Train, (d)–(f) NICAM-SPRINTARS, and (g)–(i) RAMS.

above and again suggests much faster production of precipitation for given cloud properties. This bias is vastly improved in RAMS, where absolute values of POP for a given threshold of rain rate and cloud properties are much closer to A-Train statistics. Dependencies of POP on CDR and COT are also realistically represented in RAMS.

For the same reason as in Fig. 4, the POPs are also shown as a function of CDNC and LWP in Fig. 7, which compares the POPs for A-Train, NICAM, and RAMS for the same threshold rain rates as in Fig. 6. The A-Train observations (Figs. 7a–c) demonstrate how POP tends to systematically change with CDNC and LWP. The contours for specific values of POP are found to be tilted in a manner similar to that found in Fig. 4, again demonstrating how the dependency of POP on LWP varies with CDNC. These qualitative behaviors are also reproduced in the NICAM (Figs. 7d–f) and RAMS (Figs. 7g–i) statistics, although the NICAM POPs have much larger biases than do the RAMS statistics. The RAMS statistics are again found to be much closer to A-Train in both absolute values of POP and its dependency on CDNC and LWP.

d. Vertical microphysical structure

The results shown above illustrate how drizzle and rain formation processes in the NICAM and RAMS models compare to those observed by A-Train, using comparisons of column-integrated or column-averaged quantities such as POP, CDR, COT, CDNC, and LWP. To understand the similarities and differences among the models and the observations, we exploit the unique vertical profile capability of *CloudSat*. For this purpose, we employ a new method of combining *CloudSat* and MODIS to describe vertical growth processes of cloud particles recently developed by Suzuki et al. (2010) and Nakajima et al. (2010b), who suggested the use of in-cloud optical depth, instead of geometrical height, as a vertical coordinate system to analyze profiles of radar reflectivity Z_e.

Suzuki et al. (2010) devised a method of doing this by invoking the adiabatic growth assumption to provide a way of vertically distributing the MODIS column COT into in-cloud radar bins and then using the in-cloud optical depth (ICOD) as a vertical coordinate system to describe radar reflectivity profiles. The adiabatic model

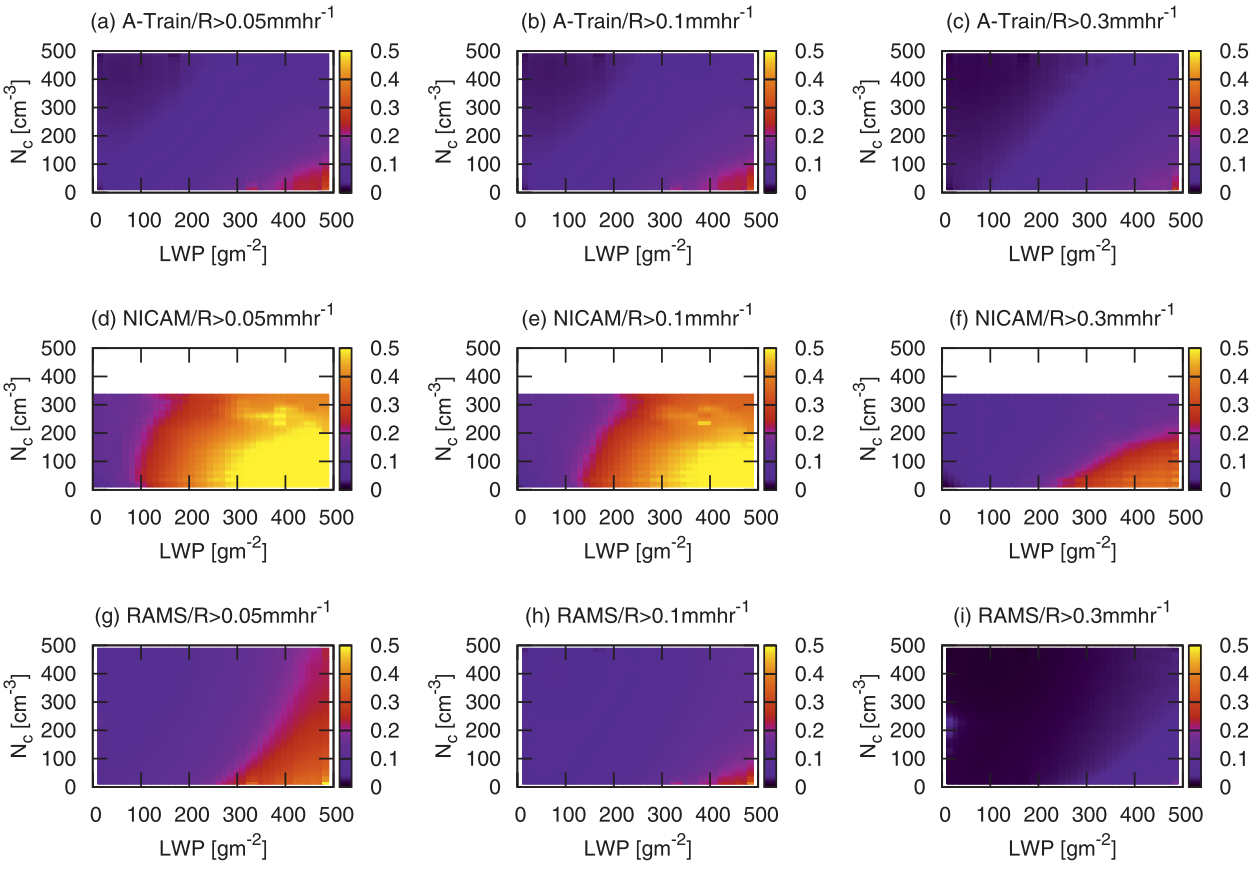

FIG. 7. POP defined with specified threshold values of precipitation rate of (left to right) 0.05, 0.1, and 0.3 mm h^{-1} as a function of CDNC and LWP obtained from (a)–(c) A-Train, (d)–(f) NICAM-SPRINTARS, and (g)–(i) RAMS.

imposes a linear increase in cloud water content with height h from the cloud base and a constancy of CDNC throughout the cloud layer. These assumptions provide a dependency of the optical thickness measured from the cloud bottom at height h as being proportional to $h^{5/3}$, leading to ICOD measured from the cloud top at height h expressed as (Suzuki et al. 2010)

$$\tau_d(h) = \tau_c\left[1 - \left(\frac{h}{H}\right)^{5/3}\right], \qquad (2)$$

where H and τ_c denotes the total geometrical thickness and the total optical thickness of the cloud layer, respectively. The former is determined from the altitudes of the radar echo top and the radar echo bottom observed by *CloudSat* whereas the latter is obtained from MODIS COT. The ICOD determined by (2) is then used as a vertical coordinate system to describe frequencies of radar reflectivity normalized at each ICOD, in the form referred to as the contoured frequency by optical depth diagram (CFODD).

This method of determining the in-cloud optical depth between the cloud top and cloud bottom contains some uncertainties as discussed in Suzuki et al. (2010). One of the uncertainties arises from the fact that *CloudSat* and MODIS do not have exactly same sensitivities to particle sizes. Under the circumstance where *CloudSat* observes large radar reflectivity near the cloud base, which is especially the case for raining clouds, the *CloudSat* echo bottom may lie below the cloud bottom corresponding to MODIS COT. Although this means that the geometrical thickness H estimated by *CloudSat* may exceed the true cloud geometrical thickness, especially for heavily drizzling or raining clouds, the total COT τ_c in (2) is constrained from MODIS and thus the ICOD determined according to (2) is limited by the observed τ_c.

Figures 8a–d present the *CloudSat* radar reflectivity profiles as classified according to MODIS-derived CDR in a manner similar to Suzuki et al. (2010). The reflectivity profiles expressed in such a form expose cloud microphysical structures that tend to vary with CDR as shown in Figs. 8a–d. Remarkable in Figs. 8a–d is the apparent trimodal characteristic of radar reflectivity

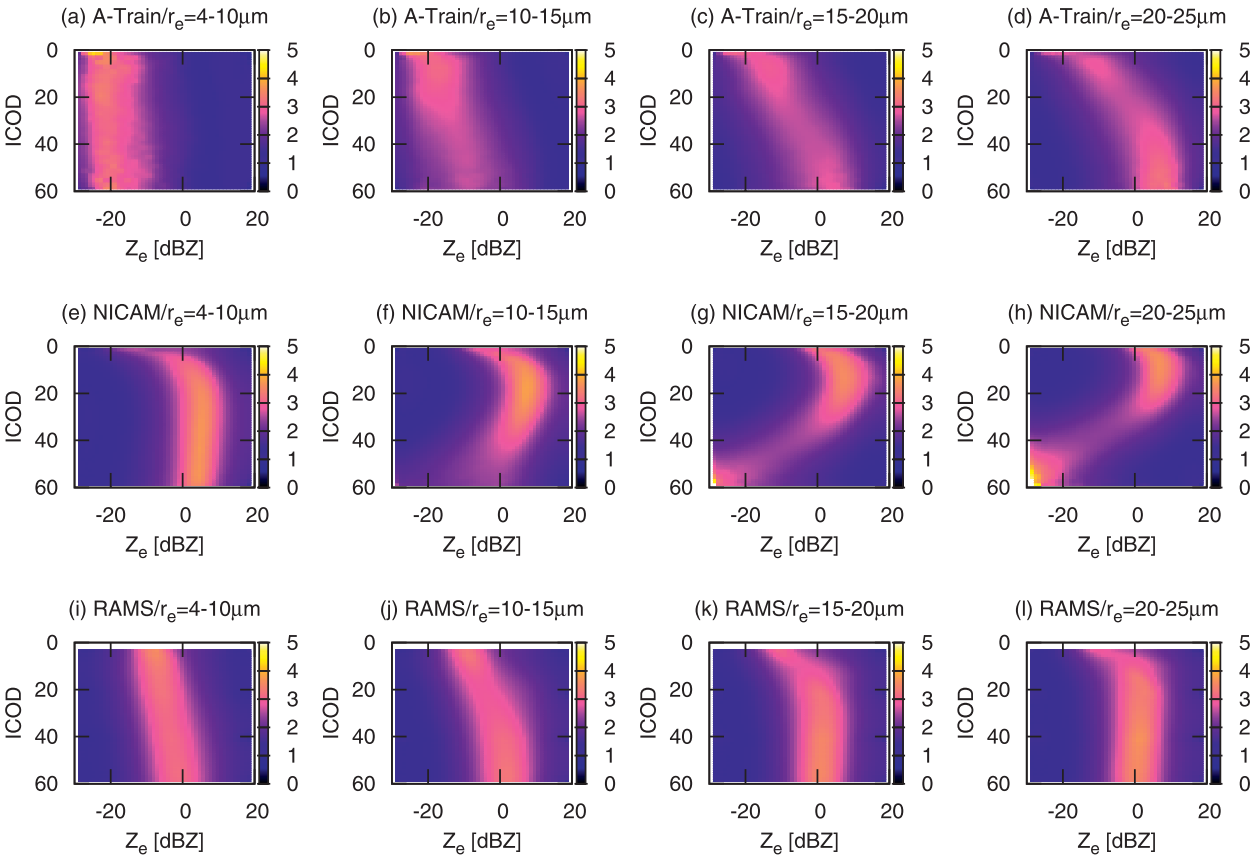

FIG. 8. Vertical profiles of radar reflectivity described as a function of in-cloud optical depth (ICOD) in the form of a contoured frequency by optical depth diagram (CFODD) grouped according to near-cloud-top effective particle radius into (left to right) 4–10, 10–15, 15–20, and 20–25 μm obtained from (a)–(d) A-Train, (e)–(h) NICAM-SPRINTARS, and (i)–(l) RAMS. The unit of color shading is % dBZ^{-1}.

broadly found in the ranges of -25 to -20, -15 to -10, and 0 to 10 dBZ, which we interpret as corresponding to cloud, drizzle, and rain particles, respectively, as argued by Suzuki et al. (2010). These modes appear to transition from one to another in a fairly monotonic way with increasing CDR. The cloud mode characterized by radar reflectivity smaller than about -20 dBZ is obvious through the entire cloud layer in Fig. 8a for CDR values smaller than 10 μm and becomes less pronounced in the lower layer when the CDR is larger than 10 μm as shown in Fig. 8b. Figures 8c and 8d show that the peak located around $Z_e = -15$ to -10 dBZ and $\tau_d = 5$ to 15 becomes pronounced when CDR exceeds 15 μm. Below this peak appears the tendency for Z_e to increase with increasing τ_d (or decreasing height), which we interpret as representing downward growth of drizzle particles falling through the cloud layer and collecting the cloud particles. The radar reflectivity increases downward, eventually reaching a value around 10 dBZ in the lowest part of the cloud layer as shown in Fig. 8d. This feature is likely to represent rain formation. These characteristics found in Figs. 8a–d illustrate that the cloud-to-rain particle growth processes are clearly evident and that the transition from cloud through drizzle to rain takes place as a fairly monotonic function of CDR (Suzuki et al. 2010; Nakajima et al. 2010b).

Figures 8e–h and 8i–l show corresponding statistics from NICAM and RAMS, respectively. The NICAM statistics clearly illustrates how fast the cloud-to-rainwater conversion occurs vertically when compared to the A-Train statistics. Even when CDR is smaller than 10 μm (Fig. 8e), the cloud water located around $Z_e = -20$ dBZ at $\tau_d < 5$ is found to transition into rainwater characterized by Z_e larger than 0 dBZ as τ_d increases. The conversion tends to become faster for ranges of larger values of CDR as shown in Figs. 8f–h. Decreasing tendencies of Z_e with increasing τ_d found in the lower part of Figs. 8g and 8h are due to the attenuation effect, indicating that a large amount of rainwater has formed in the lower cloud layer for ranges of CDR greater than 15 μm. These results suggest that NICAM qualitatively represents the monotonic increase in vertical cloud-to-rainwater conversion

with increasing CDR, although there is a large bias of the conversion rate in a quantitative sense. This is also consistent with the previous results.

This bias of NICAM is found to be vastly improved in the RAMS statistics shown in Figs. 8i–l. When CDR is smaller than 10 μm (Fig. 8i), the majority of radar reflectivity is located between -20 and 0 dBZ, which mostly belongs to the drizzle category and thus is biased toward larger values than observed (Fig. 8a) but is generally improved compared to NICAM. The reflectivities tend to become larger with increasing CDR as shown in Figs. 8j–l in a manner consistent with the A-Train observations shown in the top panels. Remarkably, the RAMS reflectivity profiles for CDR greater than 15 μm (Figs. 8k,l) are much closer to corresponding observations (Figs. 8c,d) than in NICAM (Figs. 8g,h). This suggests that the water conversion from drizzle to rain categories is more realistic in RAMS, which is also consistent with the results shown above.

5. Conclusions and discussion

This study compares the warm rain formation processes observed by *CloudSat* and MODIS satellite observations with statistics of two CRMs (i.e., NICAM and RAMS). Several methods of investigating these processes recently developed for analyzing *CloudSat* and A-Train observations are employed to evaluate and compare the model statistics with observations from *CloudSat* and MODIS. Given that the statistics shown are dictated by the cloud-to-rainwater conversion processes, the comparisons reveal a picture of the processes, both observed and modeled, and their striking differences. The observed clouds have an incipient growth stage where only cloud water exists without drizzle or precipitation as characterized by a significant fraction of the no precipitation category for the smallest values of LWP. This observed characteristic is not represented by either NICAM or RAMS, where cloud water tends to be readily converted to larger-sized particles more quickly, whichever drizzle or rainwater category represents them. This is demonstrated as equivalent behaviors between the rain category in NICAM and the drizzle plus rain categories in RAMS, although RAMS appears to partition the larger-sized water species into drizzle and rain more realistically. These model behaviors exposed by the comparison with A-Train observations point to a possible area of model improvement, namely the more realistic representation of the no precipitation regime of the clouds.

These differences in results between the two models arise from differences in several aspects of the models, including horizontal resolution, spatial scales, and cloud microphysics parameterizations for autoconversion, accretion, evaporation, and sedimentation processes. Although all of these factors may influence the results, autoconversion and accretion are among the important processes that control the water conversion process. In this regard, it is worth noting that NICAM and RAMS are based on one- and two-moment schemes, respectively, for these processes. This difference may influence the water conversion pattern through their different representation of particle size spectrum: the single-moment scheme with mode locations typically fixed inherently lacks the ability to represent the gradual water transition through drizzle, which, in principle, can be represented more flexibly by double-moment schemes given its nature of variable mode locations. This notion, however, needs to be investigated by more direct comparisons between the single- and double-moment schemes within a common model framework where other components are set exactly the same. It would be useful for this purpose to employ a single-column model approach to analyze the precipitation characteristics in terms of the phase space spanned by cloud parameters such as LWP and CDNC (e.g., Brenguier et al. 2000; Pawlowska and Brenguier 2003; vanZanten et al. 2005; Wood 2005; Wood et al. 2009) analogous also to those shown in Figs. 4 and 7. It should also be noted that the autoconversion and accretion processes are sensitive to schemes used and there exist a variety of parameterization formulas even within the single- or double-moment schemes. The optimized parameter values for a given scheme also depend on spatial scales and resolutions of models. Besides these processes, the evaporation and sedimentation processes are also important, especially when comparing the surface rainfall rate. We then need more thorough examinations covering the wide range of such parameterizations and spatial scales to obtain more robust understanding of the behaviors of model microphysics. To this end, the comparison methods demonstrated in this study would provide a useful way of diagnosing the parameterizations in terms of the cloud-to-rainwater conversion processes. Sensitivity studies of replacing the parameterization formulas and/or changing the uncertain parameters within a common framework of cloud-resolving models with the aid of such a diagnostic approach would also be useful to find, for instance, optimized parameter values and new formulations aimed at improving parameterizations, including a better representation of the no precipitation regime in the models examined.

Acknowledgments. We are grateful to Ralf Bennartz and two anonymous reviewers for their invaluable comments that greatly improved this paper. We also acknowledge Tristan L'Ecuyer and Norm Wood for fruitful

discussions and John Haynes, who provided the QuickBeam code. The *CloudSat* data products were provided by *CloudSat* Data Processing Center at CIRA/Colorado State University. This study was supported by NASA Grants NNX07AR11G and NNX09AJ45G. S. C. van den Heever was supported by the National Science Foundation under Grant ATM-0820557. T. Y. Nakajima was partly supported by the EarthCARE Science Project (2007–2010) and the GCOM-C Science Project (2009–2010) of the Japan Aerospace Exploration Agency (JAXA). The NICAM-SPRINTARS simulation was performed on the Earth Simulator with financial support of the RR2002 project by MEXT in Japan. K. Suzuki also acknowledges Tatsuya Seiki for his help to run the model.

REFERENCES

Bennartz, R., 2007: Global assessment of marine boundary layer cloud droplet number concentration from satellite. *J. Geophys. Res.,* **112,** D02201, doi:10.1029/2006JD007547.

Berg, W., T. L'Ecuyer, and S. van den Heever, 2008: Evidence for the impact of aerosols on the onset and microphysical properties of rainfall from a combination of satellite observations and cloud-resolving model simulations. *J. Geophys. Res.,* **113,** D14S23, doi:10.1029/2007JD009649.

Brenguier, J.-L., H. Pawlowska, L. Schüller, R. Preusker, J. Fischer, and Y. Fouquart, 2000: Radiative properties of boundary layer clouds: Droplet effective radius versus number concentration. *J. Atmos. Sci.,* **57,** 803–821.

Chang, F.-L., and Z. Li, 2002: Estimating the vertical variation of cloud droplet effective radius using multispectral near-infrared satellite measurements. *J. Geophys. Res.,* **107,** 4257, doi:10.1029/2001JD000766.

Cotton, W. R., and Coauthors, 2003: RAMS 2001: Current status and future directions. *Meteor. Atmos. Phys.,* **82,** 5–29.

Dufresne, J.-L., and S. Bony, 2008: An assessment of the primary sources of spread of global warming estimates from coupled atmosphere–ocean models. *J. Climate,* **21,** 5135–5144.

Feingold, G., and A. J. Heymsfield, 1992: Parameterizations of condensational growth of droplets for use in general circulation models. *J. Atmos. Sci.,* **49,** 2325–2342.

——, R. L. Walko, B. Stevens, and W. R. Cotton, 1998: Simulations of marine stratocumulus using a new microphysical parameterization scheme. *Atmos. Res.,* **47–48,** 505–528.

Grabowski, W. W., 1998: Toward cloud resolving modeling of large-scale tropical circulations: A simple cloud microphysics parameterization. *J. Atmos. Sci.,* **55,** 3283–3298.

Haynes, J. M., R. T. Marchand, Z. Luo, A. Bodas-Salcedo, and G. L. Stephens, 2007: A multipurpose radar simulation package: QuickBeam. *Bull. Amer. Meteor. Soc.,* **88,** 1723–1727.

——, T. S. L'Ecuyer, G. L. Stephens, S. D. Miller, C. Mitrescu, N. B. Wood, and S. Tanelli, 2009: Rainfall retrieval over the ocean with spaceborne W-band radar. *J. Geophys. Res.,* **114,** D00A22, doi:10.1029/2008JD009973.

Inoue, T., M. Satoh, Y. Hagihara, H. Miura, and J. Schmetz, 2010: Comparison of high-level clouds represented in a global cloud system–resolving model with CALIPSO/*CloudSat* and geostationary satellite observations. *J. Geophys. Res.,* **115,** D00H22, doi:10.1029/2009JD012371.

Kawamoto, K., T. Nakajima, and T. Y. Nakajima, 2001: A global determination of cloud microphysics with AVHRR remote sensing. *J. Climate,* **14,** 2054–2068.

Khain, A. P., M. Ovtchinnikov, M. Pinsky, A. Pokrovsky, and H. Krugliak, 2000: Notes on the state-of-the-art numerical modeling of cloud microphysics. *Atmos. Res.,* **55,** 159–224.

Kubar, T. L., D. L. Hartmann, and R. Wood, 2009: Understanding the importance of microphysics and macrophysics for warm rain in marine low clouds. Part I: Satellite observations. *J. Atmos. Sci.,* **66,** 2953–2972.

Lebsock, M. D., G. L. Stephens, and C. Kummerow, 2008: Multisensor satellite observations of aerosol effects on warm clouds. *J. Geophys. Res.,* **113,** D15205, doi:10.1029/2008JD009876.

L'Ecuyer, T. S., W. Berg, J. Haynes, M. Lebsock, and T. Takemura, 2009: Global observations of aerosol impacts on precipitation occurrence in warm maritime clouds. *J. Geophys. Res.,* **114,** D09211, doi:10.1029/2008JD011273.

Leon, D. C., Z. Wang, and D. Liu, 2008: Climatology of drizzle in marine boundary layer clouds based on 1 year of data from *CloudSat* and Cloud–Aerosol Lidar and Infrared Pathfinder Satellite Observations (CALIPSO). *J. Geophys. Res.,* **113,** D00A14, doi:10.1029/2008JD009835.

Mace, G. G., R. Marchand, Q. Zhang, and G. Stephens, 2007: Global hydrometeor occurrence as observed by *CloudSat*: Initial observations from summer 2006. *Geophys. Res. Lett.,* **34,** L09808, doi:10.1029/2006GL029017.

Marchand, R., G. G. Mace, T. Ackerman, and G. Stephens, 2008: Hydrometeor detection using *CloudSat*—An Earth-orbiting 94-GHz cloud radar. *J. Atmos. Oceanic Technol.,* **25,** 519–533.

Masunaga, H., M. Satoh, and H. Miura, 2008: A joint satellite and global cloud-resolving model analysis of a Madden–Julian oscillation event: Model diagnosis. *J. Geophys. Res.,* **113,** D17210, doi:10.1029/2008JD009986.

Meyers, M. P., R. L. Walko, J. Y. Harrington, and W. R. Cotton, 1997: New RAMS cloud microphysics parameterization. Part II: The two-moment scheme. *Atmos. Res.,* **45,** 3–39.

Miura, H., M. Satoh, T. Nasuno, A. T. Noda, and K. Oouchi, 2007: A Madden–Julian oscillation event realistically simulated by a global cloud-resolving model. *Science,* **318,** 1763–1765.

Nakajima, T., and M. D. King, 1990: Determination of the optical thickness and effective particle radius of clouds from reflected solar radiation measurements. Part I: Theory. *J. Atmos. Sci.,* **47,** 1878–1893.

Nakajima, T. Y., and T. Nakajima, 1995: Wide-area determination of cloud microphysical properties from NOAA AVHRR measurements for FIRE and ASTEX regions. *J. Atmos. Sci.,* **52,** 4043–4059.

——, K. Suzuki, and G. L. Stephens, 2010a: Droplet growth in warm water clouds observed by the A-Train. Part I: Sensitivity analysis of the MODIS-derived cloud droplet sizes. *J. Atmos. Sci.,* **67,** 1884–1896.

——, ——, and ——, 2010b: Droplet growth in warm water clouds observed by the A-Train. Part II: A multi-sensor view. *J. Atmos. Sci.,* **67,** 1897–1907.

Pawlowska, H., and J.-L. Brenguier, 2003: An observational study of drizzle formation in stratocumulus clouds for general circulation model (GCM) parameterizations. *J. Geophys. Res.,* **108,** 8630, doi:10.1029/2002JD002679.

Pielke, R. A., and Coauthors, 1992: A comprehensive meteorological modeling system—RAMS. *Meteor. Atmos. Phys.,* **49,** 69–91.

Platnick, S., 2000: Vertical photon transport in cloud remote sensing problems. *J. Geophys. Res.,* **105,** 22 919–22 935.

Rogers, R. R., and M. K. Yau, 1989: *A Short Course in Cloud Physics*. Elsevier, 293 pp.

Saleeby, S. M., and W. R. Cotton, 2004: A large-droplet mode and prognostic number concentration of cloud droplets in the Colorado State University Regional Atmospheric Modeling System (RAMS). Part I: Module descriptions and supercell test simulations. *J. Appl. Meteor.,* **43,** 182–195.

——, W. Berg, S. van den Heever, and T. L'Ecuyer, 2010: Impact of cloud-nucleating aerosols in cloud-resolving model simulations of warm-rain precipitation in the East China Sea. *J. Atmos. Sci.,* **67,** 3916–3930.

Satoh, M., T. Matsuno, H. Tomita, H. Miura, T. Nasuno, and S. Iga, 2008: Nonhydrostatic Icosahedral Atmospheric Model (NICAM) for global cloud resolving simulations. *J. Comput. Phys.,* **227,** 3486–3514.

——, T. Inoue, and H. Miura, 2010: Evaluations of cloud properties of global and local cloud system resolving models using CALIPSO and *CloudSat* simulators. *J. Geophys. Res.,* **115,** D00H14, doi:10.1029/2009JD012247.

Stephens, G. L., 2005: Cloud feedbacks in the climate system: A critical review. *J. Climate,* **18,** 237–273.

——, and J. M. Haynes, 2007: Near global observations of the warm rain coalescence process. *Geophys. Res. Lett.,* **34,** L20805, doi:10.1029/2007GL030259.

——, and Coauthors, 2002: The *CloudSat* mission and the A-Train. *Bull. Amer. Meteor. Soc.,* **83,** 1771–1790.

——, and Coauthors, 2008: The *CloudSat* mission: Performance and early science after the first year of operation. *J. Geophys. Res.,* **113,** D00A18, doi:10.1029/2008JD009982.

——, T. L'Ecuyer, R. Forbes, A. Gettleman, C. Golaz, K. Suzuki, P. Gabriel, and J. Haynes, 2010: Dreary state of precipitation in global models. *J. Geophys. Res.,* **115,** D24211, doi:10.1029/2010JD014532.

Suzuki, K., and G. L. Stephens, 2008: Global identification of warm cloud microphysical processes with combined use of A-Train observations. *Geophys. Res. Lett.,* **35,** L08805, doi:10.1029/2008GL033590.

——, and ——, 2009: Relationship between radar reflectivity and the time scale of warm rain formation in a global cloud-resolving model. *Atmos. Res.,* **92,** 411–419.

——, T. Nakajima, A. Numaguti, T. Takemura, K. Kawamoto, and A. Higurashi, 2004: A study of the aerosol effect on a cloud field with simultaneous use of GCM modeling and satellite observation. *J. Atmos. Sci.,* **61,** 179–194.

——, ——, M. Satoh, H. Tomita, T. Takemura, T. Y. Nakajima, and G. L. Stephens, 2008: Global cloud-system-resolving simulation of aerosol effect on warm clouds. *Geophys. Res. Lett.,* **35,** L19817, doi:10.1029/2008GL035449.

——, T. Y. Nakajima, and G. L. Stephens, 2010: Particle growth and drop collection efficiency of warm clouds as inferred from joint *CloudSat* and MODIS observations. *J. Atmos. Sci.,* **67,** 3019–3032.

Takemura, T., H. Okamoto, Y. Maruyama, A. Numaguti, A. Higurashi, and T. Nakajima, 2000: Global three-dimensional simulation of aerosol optical thickness distribution of various origins. *J. Geophys. Res.,* **105,** 17 853–17 873.

——, T. Nakajima, O. Dubovik, B. N. Holben, and S. Kinne, 2002: Single-scattering albedo and radiative forcing of various aerosol species with a global three-dimensional model. *J. Climate,* **15,** 333–352.

Tanelli, S., S. L. Durden, E. Im, K. S. Pak, D. G. Reinke, P. Partain, J. M. Haynes, and R. T. Marchand, 2008: *CloudSat*'s cloud profiling radar after two years in orbit: Performance, calibration and processing. *IEEE Trans. Geosci. Remote Sens.,* **46,** 3560–3573.

Tomita, H., and M. Satoh, 2004: A new dynamical framework of nonhydrostatic global model using the icosahedral grid. *Fluid Dyn. Res.,* **34,** 357–400.

van den Heever, S. C., G. L. Stephens, and N. B. Wood, 2011: Aerosol indirect effects on tropical convection characteristics under conditions of radiative–convective equilibrium. *J. Atmos. Sci.,* **68,** 699–718.

vanZanten, M. C., B. Stevens, G. Vali, and D. H. Lenschow, 2005: Observations of drizzle in nocturnal marine stratocumulus. *J. Atmos. Sci.,* **62,** 88–106.

Wood, R., 2005: Drizzle in stratiform boundary layer clouds. Part I: Vertical and horizontal structure. *J. Atmos. Sci.,* **62,** 3011–3033.

——, T. Kubar, and D. Hartmann, 2009: Understanding the importance of microphysics and macrophysics for warm rain in marine low clouds. Part II: Heuristic models of rain formation. *J. Atmos. Sci.,* **66,** 2973–2990.